IEEE Access
Multidisciplinary | Rapid Review | Open Access Journal

Received October 20, 2020, accepted November 3, 2020, date of publication November 16, 2020,
date of current version November 24, 2020.

Digital Object Identifier 10.1109/ACCESS.2020.3037648

A Solid State Plasma Multifunctional Metamaterial and Its Application for Energy Absorbing and Cross Polarization Conversion

LI ZENG[1], XING-LIANG TIAN[1], YU-PENG LI[1], DAN ZHANG[2], (Member, IEEE), AND HAI-FENG ZHANG[1,2,3,4], (Member, IEEE)

[1]College of Electronic and Optical Engineering and College of Microelectronics, Nanjing University of Posts and Telecommunications, Nanjing 210023, China
[2]College of Information Science and Technology, Nanjing Forestry University, Nanjing 210037, China
[3]Key Laboratory of Radar Imaging and Microwave Photonics (Nanjing Univ. Aeronaut. Astronaut.), Ministry of Education, Nanjing University of Aeronautics and Astronautics, Nanjing 210016, China
[4]State Key Laboratory of Millimeter Waves, Southeast University, Nanjing 210096, China

Corresponding author: Hai-Feng Zhang (hanlor@163.com)

This work was supported in part by the Open Research Program in China's State Key Laboratory of Millimeter Waves under Grant K201927, and in part by the Postgraduate Research and Practice Innovation Program of Jiangsu Province under Grant KYCX19_0958.

ABSTRACT With the increasing expectations of electromagnetic devices, the defects of monofunctional devices that are susceptibly limited by external constraints are becoming more and more obvious and the integration of multiple functions has gradually become the pursuit of researchers. In this paper, a novel multifunctional metamaterial tailored by the solid state plasma (SSP) is proposed. By inspiring the particular SSP resonators, such a metamaterial can be handily switched back and forth among two functions and form three working states. When the proposed SSP metamaterial is served in State I, its function embodies as an energy absorber and the absorption which is over 90% for TE and TM modes are 5.84-7.30 GHz and 5.41-6.34 GHz whose relative bandwidths (RBs) are 22.22% and 15.83%, respectively. States II and III keep the same functionality of cross-polarization conversion but a distinct operating band. The polarization conversion rate (PCR) of State II which is higher than 90% is 7.40-12.20 GHz (the RB is 48.98%) and this operational range will be shifted to 5.71-8.47 GHz (the RB is 38.92%) after switching to State III. Compared with the conventional tunable devices, this SSP metamaterial has the advantage of functional diversity and it provides a new design idea of absorber and polarization converter to promote potential applications of multifunctional devices.

INDEX TERMS Metamaterial, solid state plasma, absorber, polarization converter, tunability.

I. INTRODUCTION

The polarization state is a crucial characteristic of the electromagnetic wave (EMW) in the transmission process [1]. How to effectively manipulate polarization state has become a focus of contemporary researches. As a functional device to aim at this matter, polarization converter plays an essential standing in the manipulation of EMW, which provides the extensive potential applications in the design of circularly polarized antennas [2], [3] and radomes [4], [5], especially in the territories of nano photon devices [6] and advanced sensors [7], [8]. The conventional methods of controlling electromagnetic polarization are generally taken birefringence effect as a foundation, which are realized by dichroic solid crystal [9] and twisted nematic liquid crystal [10]. Such complex design processes of these conventional devices usually lead to an ending of cumbersome volume, and the requirements for materials and processing technology are very demanding.

Meanwhile, absorber, as a facility that can effectively absorb or harvest the energy of the incident EMW with a specific wavelength and convert it into ohmic heat or other forms of energy, emerges as the times require and owns momentous significance to reduce the radar cross-section [11], [12] and

The associate editor coordinating the review of this manuscript and approving it for publication was Amedeo Andreotti.

further improve the stealth performance [13], [14] of the designated target. In the current stage, the crux of the matter is focused on how to find out an absorbing material with high efficiency, good stability, lightweight, and thin thickness.

In recent years, metamaterials, synthetic composite structures own fantastic physical properties and functions, are explored to manipulate the transmitting EMW [15], [16]. The emergence of metamaterials develops researchers fresh design ideas in the field of science and technology. The metamaterial-based polarization converters and absorbers can effectively solve the problems as mentioned above. In 2015, an ultra-wideband metamaterial polarization converter which can realize the linear-to-linear polarization convention is presented by Gao *et al.* [17] and its relative bandwidth (RB) can reach 77.11%. In 2018, Qi *et al.* [18] proposed a double symmetrical W-shaped structure to obtain reflected circularly polarized waves. In the same year, Mishra *et al.* [19] used a fractal structure to realize the absorption band enhancement. The special sub-wavelength structure and stunning physical features of metamaterials-based polarization converters and absorbers not only can make great achievements in ultra-thin and miniaturized devices but also meet the requirements of broadband and reconfigurable features.

However, with the increasing expectations of electromagnetic devices, the performance of the monofunctional device is so susceptible that its application environments are quite restricted, which appears fatigues to meet the rapid growth of today's technological development. Their fixed structure will result in a single function and an untunable operating band so that it is hard to realize an extensive range of applications. Therefore, the tunable multifunctional devices start to appear on the stage due to the extraordinary adaptability to complex electromagnetic environments, and as a popular material with the excellent tunability and high integration, solid state plasma (SSP) is pretty suitable for solving this problem.

As a popular material with the excellent tunability and high integration, solid state plasma (SSP) is pretty suitable for solving this problem. By applying different external bias excitations on SSP which can be controlled by programming, it behaves similarly to the metallic properties when the concentration of the internal carrier increases to a certain extent. On the contrary, the low carrier concentration caused by low voltage will lead the SSP to an unexcited eigenstate with little ability to carry the EMW (equivalent to dielectric). Therefore, the exceptional reconfigurability can be obtained by artificially inspiring SSP with various structures and positions [20]–[22].

In military field, electromagnetic shielding [23], [24] and polarization manipulating [25], [26] have always been the hot topic for researcher. For some specific scenarios, when these two functions are both taken into account [27], [28], especially for radome detection, electromagnetic compatibility, electromagnetic interference and anti-interference, and other military fields. The reconfigurable design such as compatibility of multiple functions and dynamic tuning of operating band will be a inevitable trend of development. This kind of integrated multi-functional device is extremely necessary and also has great potential application value in miniaturization design. How to integrate a variety of closely related electromagnetic auxiliary equipment with special functions is one of the problems that this paper attempts to explore and solve.

In this paper, a novel multifunctional metamaterial tailored by SSP is presented, which contains two SSP resonance layers. After the special design, three operating states can be realized by exciting the SSP resonators in different regions and the proposed SSP metamaterial not only can switch functions between absorber and cross-polarization converter but also can obtain a tunability operating band of polarization conversion. Such a SSP metamaterial has the advantages of wide bandwidth, multiple functions, and flexible design, which provides a new idea for the design and development of multifunctional devices with miniaturization.

II. STRUCTURE DESIGN

The schematic configuration of the unit cell for the presented SSP metamaterial is given in Fig.1. As shown in Figs.1(a) and (b), the proposed SSP metamaterial contains two SSP resonance layers. The first resonant layer consists chiefly of a pair of L-shaped SSP resonators and an Archimedean spiral SSP resonator. As for the second resonant layer, another pair of L-shaped SSP resonators and a reverse Archimedean spiral SSP resonator are involved. The radius ratio α (the ratio of the final radius to the initial radius before and after spiral rotation) and the turns number N of two helical SSP resonators are 5.8 and 5, respectively. The L-shaped SSP patched on each layer are symmetrical to each other along the diagonal. There are two FR4 dielectric layers embedded among the copper film and two SSP resonance layers with the relative permittivity of 4.3 and the dielectric loss tangent of 0.025. The unit cell of such a multifunctional SSP metamaterial is periodically tiled on the copper film with the conductivity of 5.8×10^7 S/m, and the detailed structural parameters can be inquired in Table 1.

TABLE 1. The structural parameters of the proposed SSP metamaterial.

Parameters	a	b	c	d	e	f
Value (mm)	1.7	7.4	0.54	2.4	5.8	1
Parameters	g	h_1	h_2	p	r	
Value (mm)	1.4	0.1	1.8	17	0.58	

By electric stimulating the high resistivity semiconductor films with various configuration coated proactively on the dielectric surface, the surface PIN (S-PIN) diodes are excited to form the collective effect characteristics of plasma when the charge carrier reaches sufficient concentration, which is so-called the SSP. By selectively applying the bias voltages, the SSP in different regions will be excited to

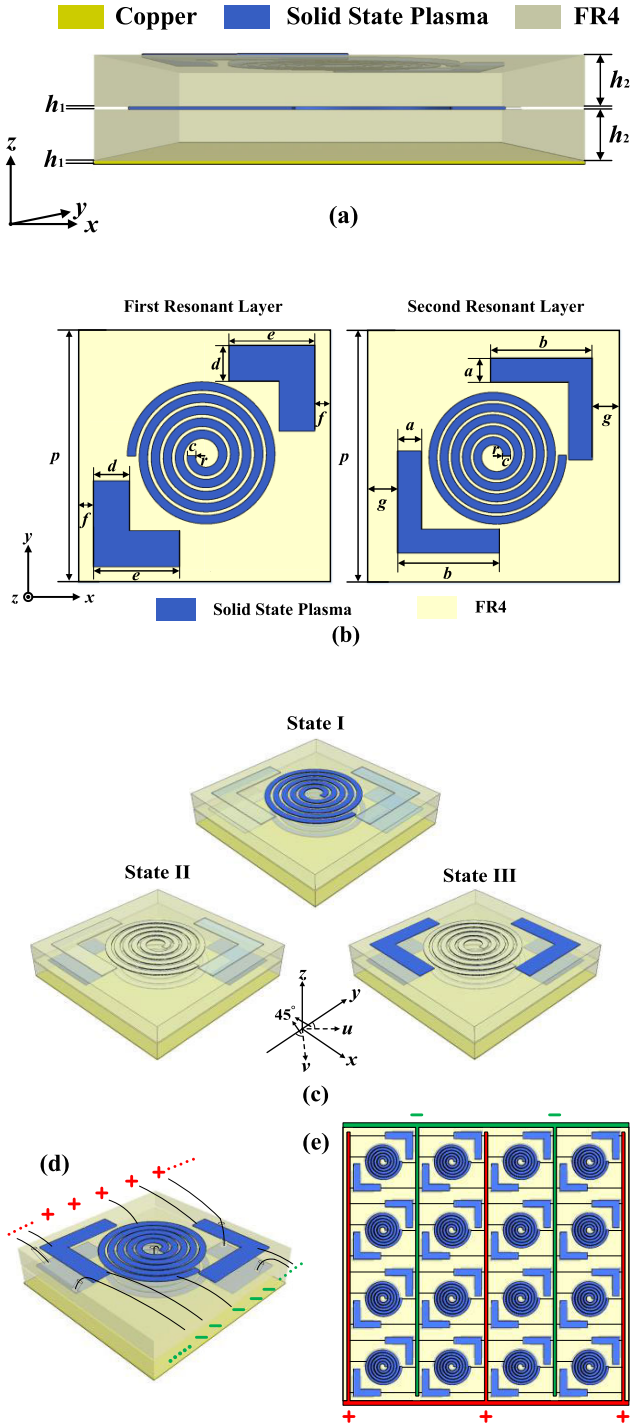

FIGURE 1. Schematic views of the unit cell for the proposed SSP metamaterial: (a) the side view of the unit cell, (b) the front view of the unit cell, (c) the diagrammatic sketch in State I, State II and State III, (d) the feeder arrangement of the unit cell, and (e) The electrode arrangement of the periodic array.

exhibit metal-like properties, thus realizing the tunability. By learning from the relevant literature [26], [29] excitation methods adopted for periodic structure and deriving inspiration from it, the schematic configuration of the conducting embodiment is presented in Figs.1 (d) and (e). For the

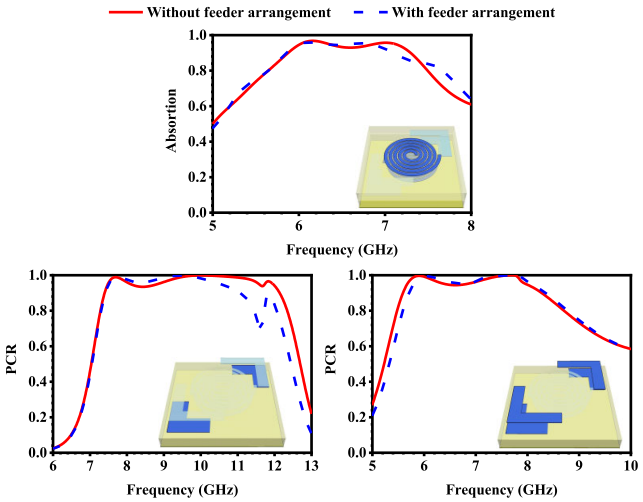

FIGURE 2. The comparison results with and without the feeder arrangement.

periodic structure, the positive and negative slender metal electrodes are alternately set on the left and right sides of each unit cells, and each solid state plasma resonator can be powered by the uniform voltage applied at the edges of the periodic array. In detail, some through-holes are drilled in the specific position of the second layer dielectric for the introduction of the feeders to inspire the solid state plasma resonators in the intermediate layer. The feeder arrangements of an adjacent unit cell along the horizontal direction are symmetrical to each other, but the same in the vertical direction. Due to the need of expensive cost and precise experimental environment, the reconfigurability of solid-state plasma for multi-functional devices is explored in theory without the experimental validation. The comparison results with and without the feeder arrangement are shown in Fig. 2. We can see that the two curves are basically consistent in each states. The deviation in the details brought by the feeder arrangement is inevitable, but on the whole, we can still draw the conclusion that the proposed multi-functional metamaterial can achieve efficient tunability and the results have been as close to the reality as possible.

After the special design, we can see clearly from Fig.1(c) that three operating states can be realized by exciting the SSP resonators in different regions (for a more distinctive demonstration, the second dielectric layer is hidden and the uninspired SSP resonators are faded). On the one hand, when only two helical SSP resonators with opposite rotations are excited, such a SSP metamaterial can act as an energy absorber and this case is called State I. On the other hand, if merely two L-shaped SSP resonators located on the first dielectric layer are inspired (such a case is named State II), the function of our design is switched to realize the cross-polarization conversion. Further, based on State II, when two L-shaped SSP resonators on the second layer are also motivated (we call this case State III), the corresponding operating band will be shifted to the low-frequency region while holding on the function of State II.

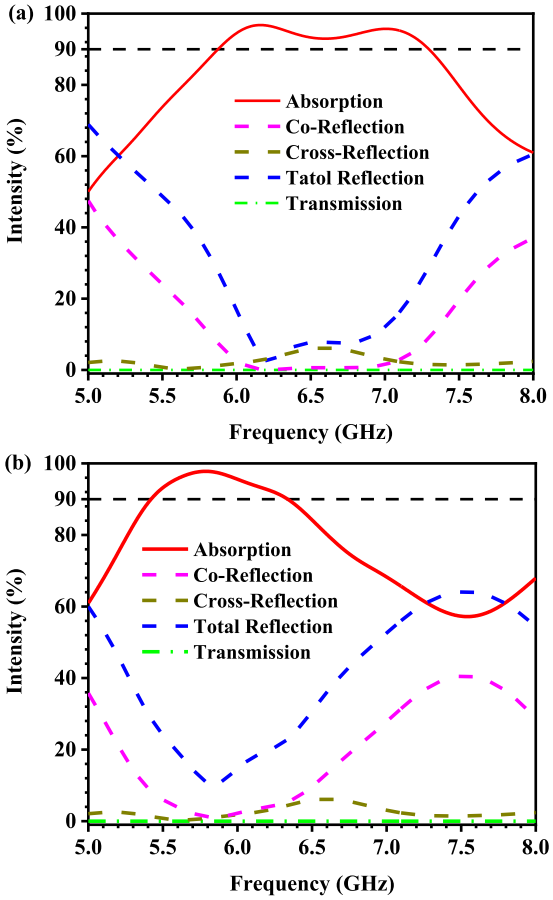

FIGURE 3. The absorption, co-reflection, cross-reflection, total reflection, and transmission spectra of the proposed SSP metamaterial in State I: (a) TE mode, and (b) TM mode.

The permittivity of SSP is frequency-dependent which can be described by Drude model $\varepsilon_p(\omega) = 12.4 - \omega_p/(\omega^2 + j\omega\omega_c)$ [20]–[22]. The plasma frequency of two helical and four L-shaped SSP patches are $\omega_{p1} = 2.9 \times 10^{14}$ rad/s and $\omega_{p2} = 1.2 \times 10^{15}$ rad/s, respectively. The collision frequencies of all SSP resonators are $\omega_c = 1.65 \times 10^{13}$ 1/s. The Master/Slave boundary conditions are used in both the x and y directions to simulate periodic distribution, and the incident EMW is propagated along the -z-axis and illuminated the presented SSP metamaterial. The TE mode means that the electric field and magnetic field is along the y-axis and x-axis, respectively, and the directions of TM mode electric field and magnetic field are exactly opposite. All the following results in this paper are computed by the software HFSS (High Frequency Structure Simulator developed by Ansoft).

III. NUMERICAL RESULTS AND DISCUSSION OF STATE I

The first to come is the configuration introduction of State I. Thanks to the continuous ground copper coating, none incident EMW can be pierced through the double helix energy absorber. As a result of this, the derivation formula of the frequency-dependent absorption is obtained which can be written as $A(\omega) = 1 - R(\omega) - T(\omega) = 1 - R(\omega) = 1 - |S_{11}|^2$, where $A(\omega)$, $R(\omega)$ (i.e. $|S_{11}|^2$) and $T(\omega)$ are absorption, reflectivity, and transmissivity, respectively. Figs.3(a) and (b) depict the transmission, co-reflection, cross-reflection, total reflection, and absorption performances of such an absorber for the TE and TM modes, respectively. The simulated results show that absorption bands which higher than 90% are located at 5.84-7.30 GHz for TE mode, and 5.41-6.34 GHz for TM mode, whose RBs are 22.22% and 15.83%, respectively. We can notice that the cross-reflection coefficient keeps a very weak value below 0.1 throughout, and this is attributed to the 180 ° reverse configuration of two spiral resonators, which will effectively reduce the phenomenon of cross-polarization conversion.

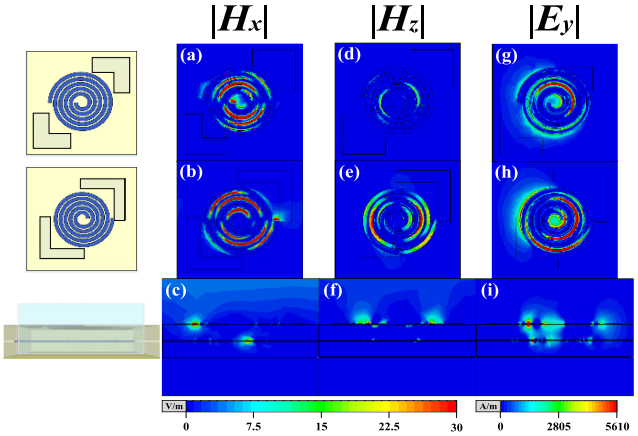

FIGURE 4. The electromagnetic field intensity distributions of the proposed SSP metamaterial at 6.23 GHz in State I for TE mode: (a)-(c) the distributions of $|H_x|$, (d)-(f) the distributions of $|H_z|$, and (g)-(i) the distributions of $|E_y|$.

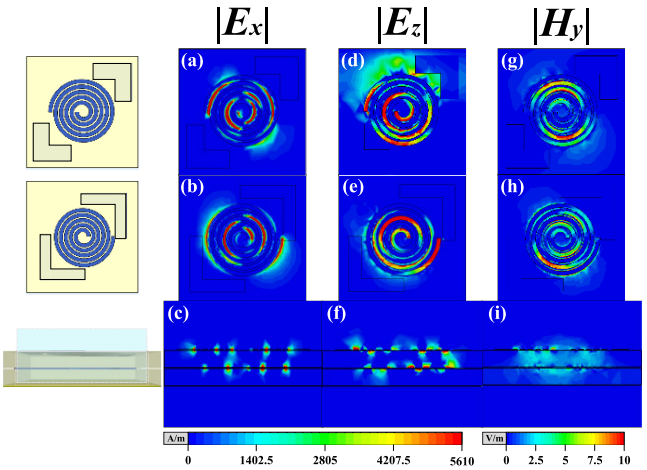

FIGURE 5. The electromagnetic field intensity distributions of the proposed SSP metamaterial at 6.23 GHz in State I for TM mode: (a)-(c) the distributions of $|E_x|$, (d)-(f) the distributions of $|E_z|$, and (g)-(i) the distributions of $|H_y|$.

To get a deep-going comprehension of the energy absorption mechanisms for TE and TM modes in State I, the electromagnetic field intensity distributions at 6.23 GHz are displayed in Figs.4 and 5, where the illustrations on the

left describe the schematic of the two resonant layers and the cross-section. Based on our definition of TE polarization mode, its effective non-zero field components are considered to be $\boldsymbol{H_x}$, $\boldsymbol{H_z}$, and $\boldsymbol{E_y}$. In contrast, the non-zero field components of TM polarization mode are corresponded to be $\boldsymbol{E_x}$, $\boldsymbol{E_z}$, and $\boldsymbol{H_y}$, respectively. As exhibited in Figs.4(a)-(c), the magnetic field intensities $|\boldsymbol{H_x}|$ are generated on the SSP-air and SSP-dielectric interfaces, and mainly localized in various arcuate gaps formed by the spiral itself, which show strong capacitive characteristics C. But there are some differences in Figs.4(d)-(f), the magnetic field resonances $|\boldsymbol{H_z}|$ mainly occur at SSP-air interface and concentrated on the SSP helix resonators, which result in the effects of inductances L. Under this circumstance, an LC equivalent circuit can be constructed to investigate the absorption mechanism [30], [31], and thus, the radius ratio α and helical width c will be discussed in detail later to adjust the values of capacitance and inductance of the equivalent circuit. Figs.4(g)-(i) reveal the electric field distributions of $|\boldsymbol{E_y}|$ and we found that $|\boldsymbol{E_y}|$ are primarily located at the first SSP layer and a small amount in the second SSP layer. It is noteworthy that $|\boldsymbol{E_y}|$ also has a certain amount of distribution in the dielectric layer between two SSP helix structures, and that means the EMWs will be reflected back and forth in this dielectric to cause energy dissipation. The analysis for TM polarization field components $|\boldsymbol{E_x}|$, $|\boldsymbol{E_z}|$ and $|\boldsymbol{H_y}|$ in Figs.5(a)-(i) take no need to go into details due to the similar principle explanation as mentioned above.

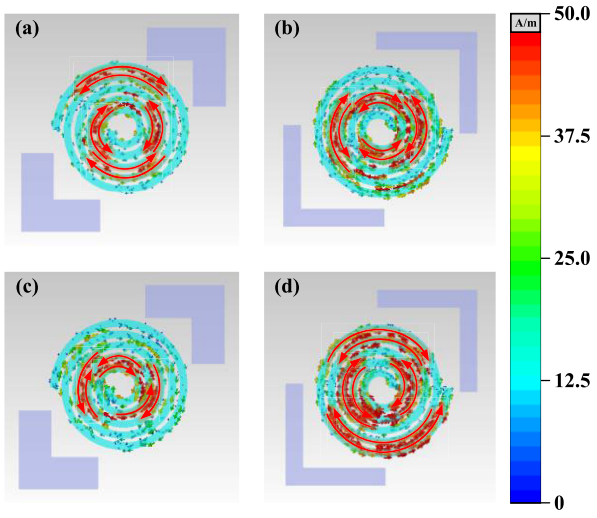

FIGURE 6. The surface current distributions on two spirals at 6.21 GHz and 6.83 GHz: (a)-(b) At 6.21 GHz, and (c)-(d) At 6.83 GHz.

Furthermore, the physical mechanism elaborated by the surface currents at 6.21 GHz and 6.93 GHz in State I have been discussed in Figs.6(a)-(b) and Figs.6(c)-(d), where the main localization and the flow directions have been marked by red arrows. We can see that the surface currents are mainly accumulated at the edges of the spiral arm, which is basically corresponded to the distributions of the electromagnetic field. It is noteworthy that the antiparallel surface current pairs are observed in adjacent spiral arms. With the enlargement of frequency, it can be found that the main contribution of the antiparallel surface current pairs are gradually extended from the central region of the spiral to the whole. Meanwhile, by combining the analysis of the electric field, magnetic field and loss density distribution in the revised manuscript, the effective coupling resonance has been verified between the two helices, which leads to the broadband energy absorption.

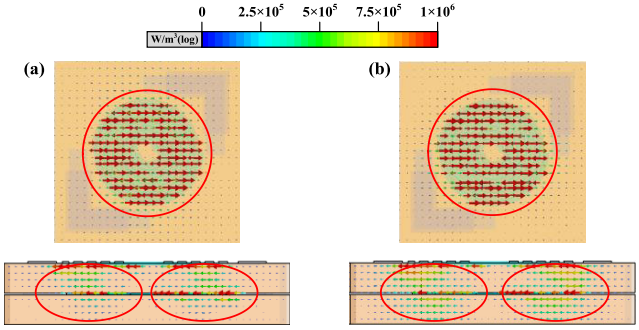

FIGURE 7. The power loss density distributions of the proposed SSP metamaterial at 7 GHz in State I: (a) for TE mode, and (b) for TM mode.

To get a more intuitive and clear cognition of the generative principle and distribution location of the energy dissipation, the power loss density distributions of the proposed SSP metamaterial at 7 GHz in State I for TE and TM modes are illustrated in Fig.5. Whether for TE or TM mode, the distributions of power loss density indicated in Figs.7(a) and (b) keep a general resemblance with small differences. It can be seen that the energy loss vectors are concentrated on the spiral structures in quantities, and the rest of the SSP resonators without excitation are acted like a dielectric. From the cross-section at the center, the losses are essentially localized in two spiral SSP resonators, but it should be noted that there is a part of consumptions permeating in two dielectric layers, especially the upper one. Therefore, the EMW will be reflected back and forth among two dielectric layers and the ground copper coating, repeatedly, which leads to the Fabry-Perot-induced mode absorption resonance.

To further understand the individual contributions of the top and bottom layer in the absorbing state. The reflection and absorption of State I have been simulated in Fig.8 when only the first spiral resonator or the second spiral resonator is excited. On the one hand, we can see that only a narrow bandwidth of absorption can be realized from 6.02 GHz to 6.28 GHz when only the first spiral is excited. But on the other, when only the second spiral is excited, the influence of asymmetric structure begins to show some embodiment and the cross-polarized reflection has reached about 20%. Therefore, the upper and lower spiral resonators are inspired simultaneously to produce a broadband absorption effect. When the two spiral resonators are vertically cascaded with each other, the interlayer coupling effect takes the dominant position, thus sublimating the individual electromagnetic response

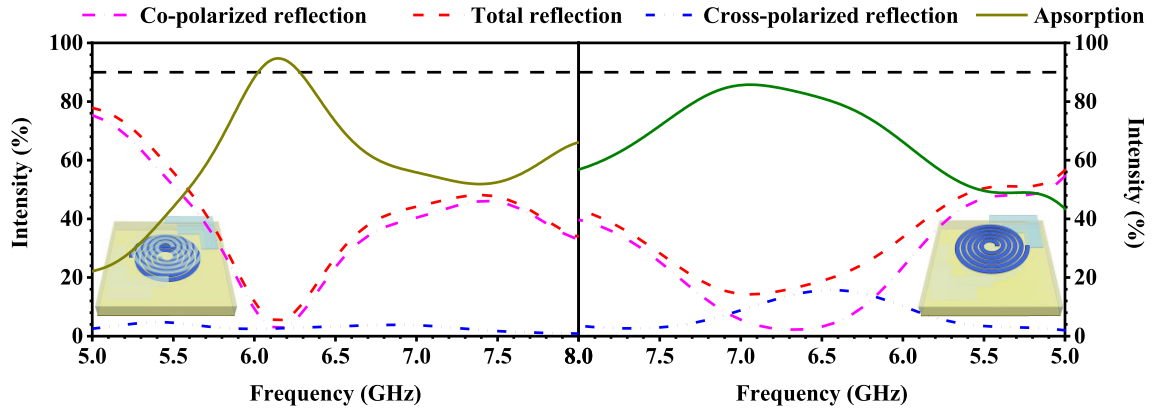

FIGURE 8. The individual contributions of reflection and absorption in State I: (a) Only the first spiral resonator is excited, and (b) Only the second spiral resonator is excited.

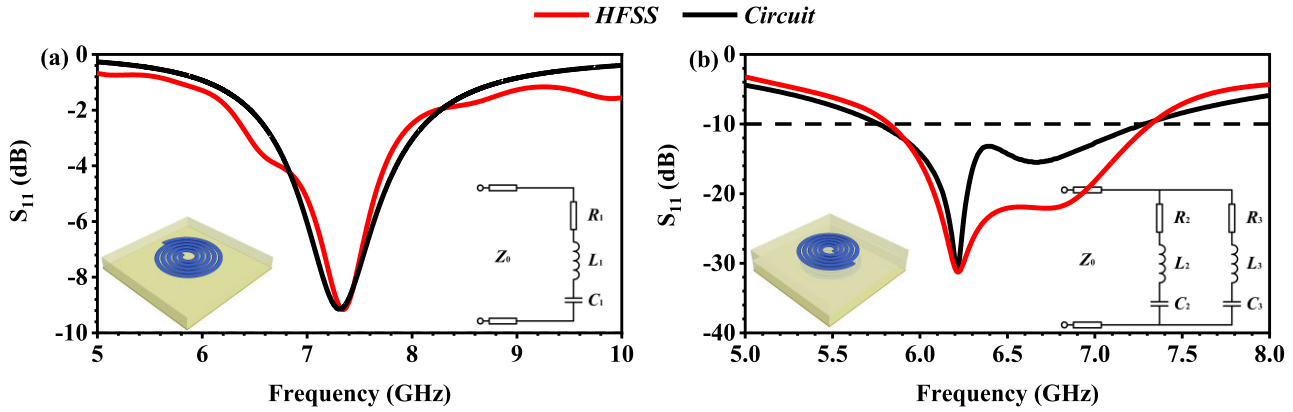

FIGURE 9. The equivalent circuit models and calculation results of single-layer spiral structure and double-layer spiral structure: (a) Single-layer spiral structure, and (b) Double-layer spiral structure.

caused by a single spiral resonator. Meanwhile, the results also prove that the 180 ° reverse configuration of two spiral resonators will effectively reduce the cross-polarized reflection.

Meanwhile, we construct the equivalent circuit model for the absorber state. First, we start with the single-layer spiral structure and the equivalent circuit model and calculation results are shown in Fig.9(a). By referencing the procedure and equations of the shunt inductive reactance and the capacitive susceptance in literature [32], the values of equivalent inductance(L_1), capacitance(C_1), and resistance(R_1) are determined as 15.857 nH, 29.9 fF, 53.6 Ω, respectively. It can be seen from the Fig.9(a) that the S-parameter curves calculated by HFSS full-wave simulation and equivalent circuit model simulation are more consistent in terms of the resonant position and intensity. However, due to the sinuosity and complexity of the spiral structure itself, a certain mutual inductance coupling effect will be brought by the spiral structure, which leads to the deviation of the S-parameter in the high-frequency region. Such a phenomenon is more obvious in the double helix structure. The equivalent circuit model and calculation results of the double-layer spiral structure are shown in Fig.9(b) and the details of equivalent component parameters are enumerated in Table 2. Although there is a certain deviation in the depth of resonance, the integrity and consistency of the frequency region with S parameter less than -10 dB are guaranteed as much as possible.

TABLE 2. The equivalent circuit parameters.

Single-helix		Double-helix			
Parameter	Value	Parameter	Value	Parameter	Value
L_1	15.86 nH	L_2	12.64 nH	L_3	5.42 nH
C_1	29.9 fF	C_2	51.9 fF	C_3	106.5 fF
R_1	53.6 Ω	R_2	3 Ω	R_3	21.76 Ω

Causing the dependence on the incident angle (IA) is a key factor to evaluate the performance of an absorber, we investigate the effects of various IAs on the absorption spectra for TE and TM modes, which summarizes in Figs.10(a) and (b), respectively. As depicted in Fig.10(a),

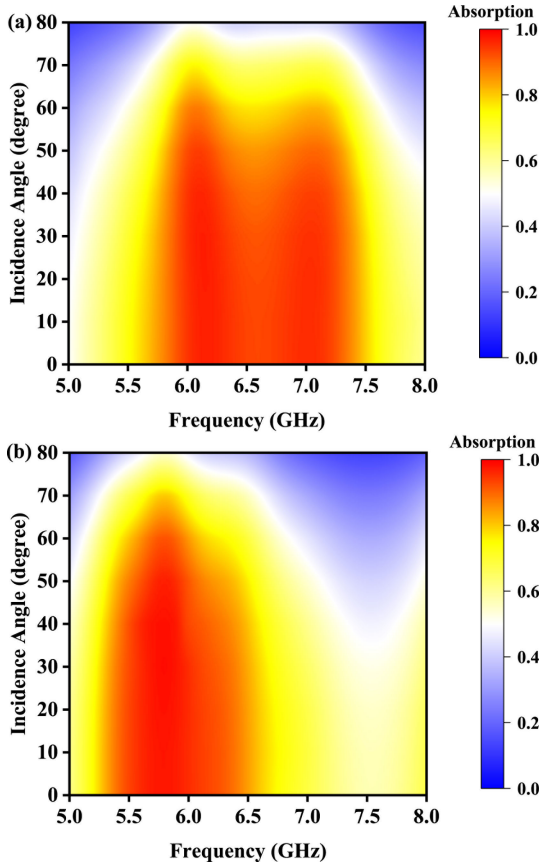

FIGURE 10. The absorption spectra of the proposed SSP metamaterial various with different IAs in State I: (a) for TE mode, and (b) for TM mode.

the absorption bandwidth above 0.9 is maintained invariant under TE mode when the IA rises from 0 ° to 40 °. As the IA continues to increase, a slight deterioration will happen in the central area of the operating band. But this deterioration is so tardy that the overall absorption remains above 0.8 in the band of 5.85-7.3 GHz when the IA reaches 55 °. For TM mode, as displayed in Fig.10(b), the same IA threshold for TM mode to keep the band (above 0.9) generally unchanged is 50 °. Until the IA exceeds 70 °, the absorption band is holistically dropped below 0.8. For both polarization modes, with the enlargement of IA, there is almost no obvious blueshift or redshift for the overall absorption band, which possesses great potential application value on many occasions. In summary, a prominent large-IA operating capabilities is proved by Figs.10(a) and (b), and such robustness is determined by the stability characteristic brought by Archimedes spiral structure itself [33].

In terms of the optimization ideas of structural parameters as described above, the relationships between the absorption performance and parameters α and c under TE mode are presented in Fig.11. As shown in Fig.11(a), by the regulating radius ratio α, the width of the internal gap of the spiral can be adjusted. When α is changed from 5.4 to 6.0, the RBs of the absorption frequency ranges are simulated to be 20.29%, 21.69%, 22.2%, and 21.8%, respectively, which

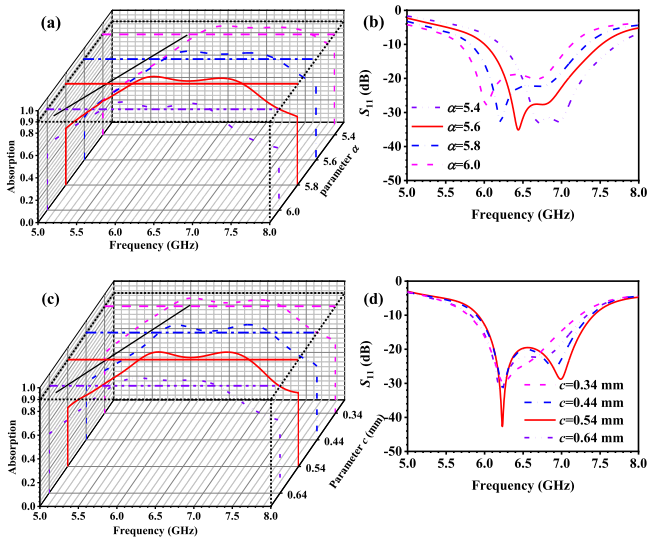

FIGURE 11. The absorption and S parameter spectra of the proposed SSP metamaterial under TE mode various with different parameters α and c in State I: (a) $\alpha = 5.4, 5.6, 5.8$ and 6.0, and (b) $c = 0.34$ mm, 0.44 mm, 0.54 mm and 0.64mm.

shows a trend of ascending first and then descending. The similar phenomena can be observed from the optimization of spiral width c (see Fig.11(c)). When c is increased from 0.34 mm to 0.54 mm, the operating band presents a tendency of muted growth and declines suddenly at 0.64 mm. In general, the selection scope of c seems to be more abundant. From Fig.11(b), we can see that two adjacent resonance points of S parameter gradually separate, and at the same time, the overall working frequency band tends to shift to the low-frequency region. Similar phenomena can be seen from the Fig.11(b), the increase of c will mainly affect the intensity of resonant frequencies, and then drive the position change of resonant frequencies. In essence, the changes of parameters α and c will lead to the changes of equivalent inductance and capacitance of the spiral structure itself, resulting in the adjustment of the S parameters and the absorption efficiency. After the overall consideration of bandwidth and absorptivity, the optimal absorption band is finally identified to be 5.84-7.30 GHz with the RB of 22.2% when $\alpha = 5.8$ and $c = 0.54$ mm.

IV. NUMERICAL RESULTS AND DISCUSSION OF STATE II AND STATE III

Since State II and State III perform the same function, the following are their unified introductions. Taking the incident wave with an electric field along the y-axis as an example, Fig.12 clearly shows the physical mechanism of cross-polarization conversion. The incident electric field can be decomposed into two mutually orthogonal components $\boldsymbol{E_{iv}}$ and $\boldsymbol{E_{iu}}$, as the formula (1) indicates. Similarly, the reflected wave is expressed as formula (2), where r_{uu} and r_{vv} are defined as the reflected coefficients on u and v axis, respectively.

$$\overrightarrow{E_i} = \overrightarrow{\boldsymbol{u}} E_{iu} \boldsymbol{e}^{\boldsymbol{j}\varphi} + \overrightarrow{\boldsymbol{v}} E_{iv} \boldsymbol{e}^{\boldsymbol{j}\varphi} \quad (1)$$

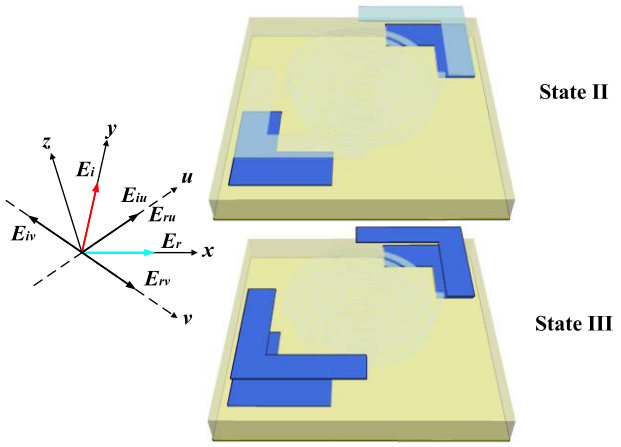

FIGURE 12. The intuitive schematic configuration of the presented SSP metamaterial in State II and State III.

$$\overrightarrow{E_r} = \overrightarrow{u}\, r_{uu} E_{ru} e^{j\varphi} + \overrightarrow{v}\, r_{vv} E_{rv} e^{j\varphi} \tag{2}$$

When r_{uu} and r_{vv} are roughly equal and their corresponding phase difference $\Delta\varphi$ is approximately around 180 °, the electric polarization direction of the reflected wave will be rotated to the x-axis.

In Figs.13(a) and (b), the reflected amplitudes r_{uu} and r_{vv} and phase difference $\Delta\varphi$ when u-polarized and v-polarized wave impact perpendicular to the proposed SSP metamaterial in State II and State III are plotted. As we expected, two conversion conditions as mentioned above are both satisfied, which can be seen in Figs.13(a) and (b), and the capabilities to realize the cross-polarization conversion in State II and State III are also preliminarily proved.

The reflected amplitudes r_{xy} and r_{yy} for the normal incidence of y-polarized waves in State II and State III are displayed in Figs.14(a) and (b), respectively. Through the equation of PCR$= r_{xy}^2/(r_{xy}^2 + r_{yy}^2 + t_{xy}^2 + t_{yy}^2)$, the curves of PCR in State II and State III are given in Fig.15. The operating frequency ranges of State II and State III are 7.4-12.2 GHz (its RB is 48.98%) and 5.71-8.47 GHz (its RB is 38.92%), respectively. Compared such two PCR curves with each other, the total operating frequency range of cross-polarization conversion can cover almost all the whole C and X bands by manual switching based on actual application requirements.

To better understand the physical principles of the cross-polarization convention in State II and State III, the surface current distributions are plotted in Figs.16(a) and (b), respectively. We can comprehend that the currents (marked by 1, 2, 4, and 5) on the L-shaped SSP resonators are opposite to those currents (marked by 3, 4, 6, and 7) on the bottom copper reflector. This case will lead to the generation of magnetic resonance, and the simultaneous existence of multiple magnetic resonances is exactly the main cause of broadband characteristics.

The cases of oblique incidence for State II and State III are also included in the investigation and the illustrations of Figs.17(a) and (b) present the PCR spectra various with

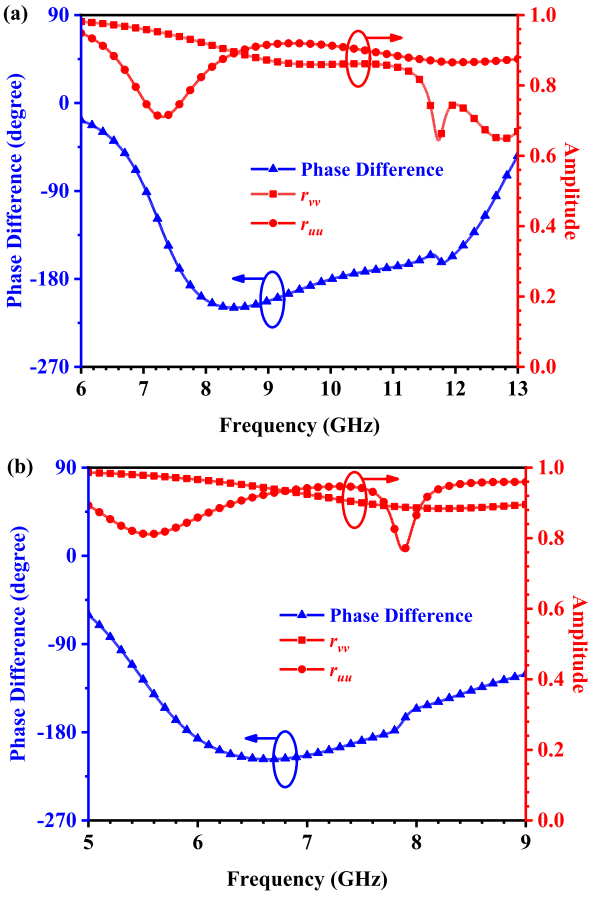

FIGURE 13. The reflected amplitudes and phase difference of the presented SSP metamaterial in State II and State III when the electric field along *u* and *v* axis: (a) State II, and (b) State III.

different IAs to us. As we can see from Fig.17(a), the operating bandwidth in State II only shows a tendency of slow coarctation, and PCR is almost kept over 0.9 when the value of IA is less than 30 °. Once IA is exceeded such a value, two obvious dips will appear in the frequency band while PCR decreases abruptly. Turn the attention to Fig.17(b), the entire working band will be split into two pieces when IA increases over 30 °. The PCR in the low-frequency region will remain as efficient as possible, while a significant deterioration will occur in the high-frequency region.

Also for State II and State III, the effects of structural parameters on PCR are taken into the discussion. In Fig.18, the alteration of arm width d of the L-shaped SSP resonators on the first resonant layer is started from 1.6 mm to 2.8 mm in State II. It can be seen from the Fig.18(b) that the co-polarized coefficient gradually decreases while two main resonance points drew closer. Accordingly, there is an enlarging trend in the cross-polarized amplitude, as shown in Fig.18(c), and this leads to the gradual optimization of PCR, which is embodied in the mergence of two separate PCR bands. The optimal operating band is available to be 7.4-12.2 GHz when d is set to be 2.4 mm.

Based on State II, the excitations of the L-shaped SSP resonators on the second resonance layer can lead to the

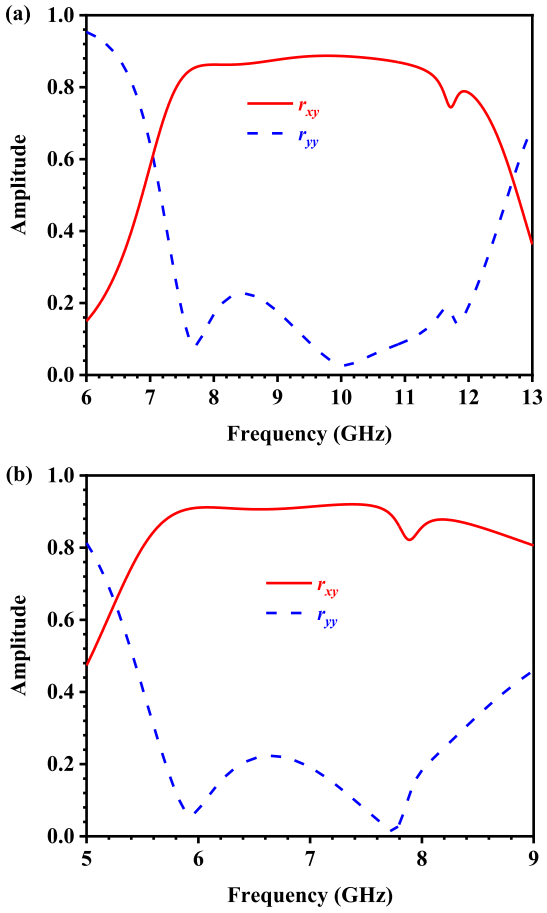

FIGURE 14. The reflected amplitudes of the proposed SSP metamaterial in State II and State III for the normal incidence of *y*-polarized wave: (a) State II, and (b) State III.

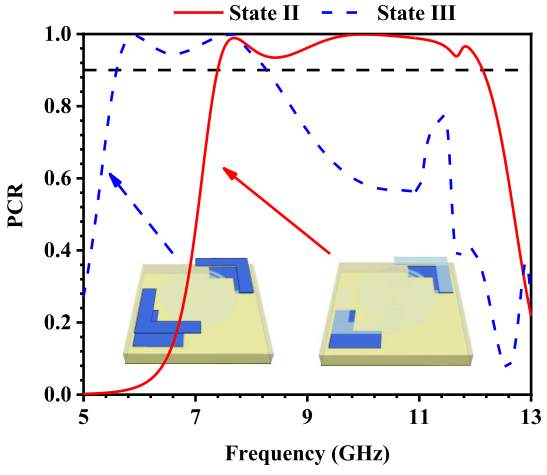

FIGURE 15. The PCR curves of the proposed SSP metamaterial in State II and State III.

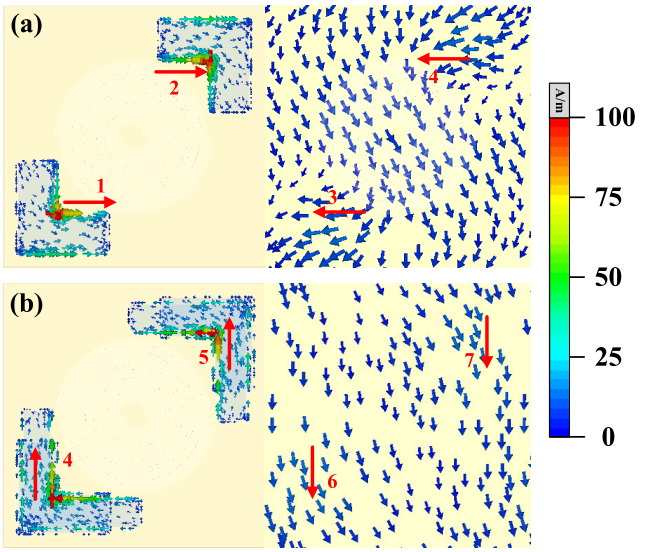

FIGURE 16. The surface current distributions of the proposed SSP metamaterial: (a) at 10 GHz in State II, and (b) at 5.93 GHz in State III.

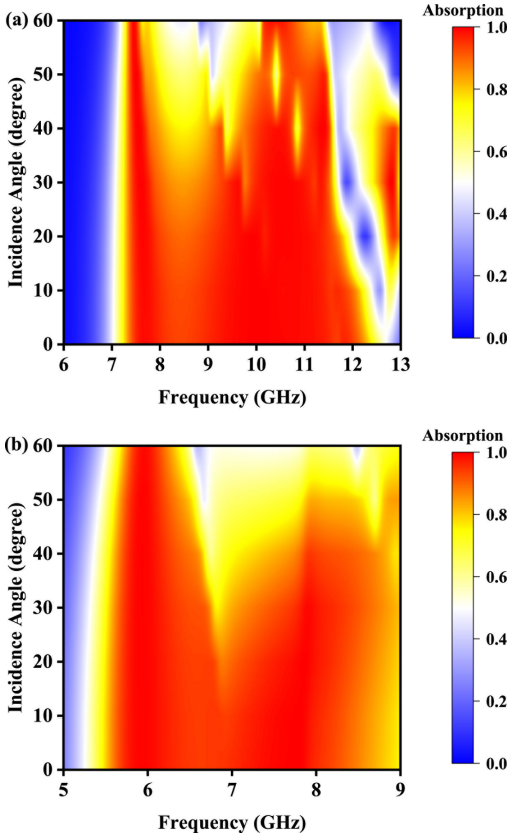

FIGURE 17. The PCR spectra of the proposed SSP metamaterial various with different IAs in State II and State III: (a) State II, and (b) State III.

shifting of the working band to the low-frequency region. Therefore, the arm width a of the L-shaped SSP resonators on the second resonant layer is deliberated in Fig.19(a), and it can be found that although the effect of a is inferior to that of d, the operating bandwidth still exists the trend of increase first and then decrease with the increasing of a. Similar phenomenons can be found in the Figs.19(b) and (c).

The alteration of the dimension of L-shaped solid state plasma resonators will affect the surface current distributions, which is one of the main reasons for the fluctuation

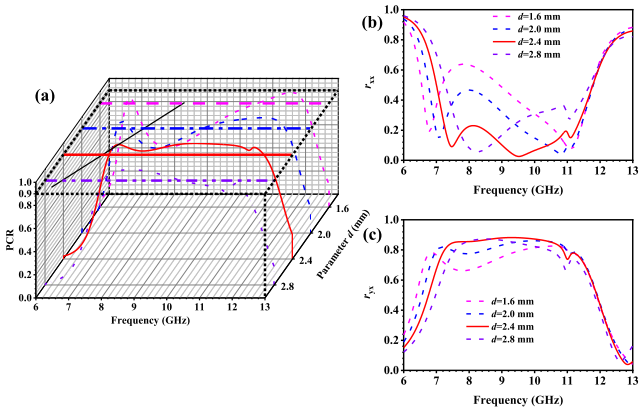

FIGURE 18. **The co-polarized coefficient, cross-polarization coefficient and PCR spectra of the proposed SSP metamaterial various with different parameters *d* in State II: (a) *PCR*, (b) Co-polarized coefficient, and (c) Cross-polarized coefficient.**

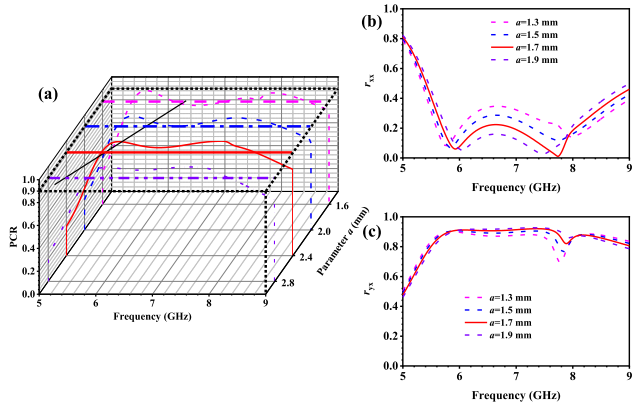

FIGURE 19. **The co-polarized coefficient, cross-polarization coefficient and PCR spectra of the proposed SSP metamaterial various with different parameters *a* in State III: (a) *PCR*, (b) Co-polarized coefficient, and (c) Cross-polarized coefficient.**

of reflection amplitudes. After comprehensive consideration of such two states, $a = 1.7$ mm and $d = 2.4$ mm is a good choice for both higher PCR and wider bandwidth.

V. CONCLUSION

In summary, an obvious means of regulation has been explored and utilized to design a multifunctional SSP metamaterial in this paper. By selectively exciting SSP resonators in different regions, the presented design is controlled to generate three operating states and realize two functions (the absorber and the cross-polarization converter). When the proposed SSP metamaterial is operating in State I, the absorption which is higher than 0.9 for TE and TM modes are situated in 5.84-7.30 GHz and 5.41-6.34 GHz, and their RBs are 22.22% and 15.83%, respectively. When such a SSP metamaterial is switched to State II, the cross-polarized wave conversion can be obtained in 7.4-12.2 GHz (the RB is 48.98%) where the PCR is above 0.9. As an extended state, the shifting phenomenon of the operating band to the lower-frequency region can be realized in State III and the corresponding PCR is shifted to 5.71-8.47 GHz whose RB is 38.92%. The influences of electromagnetic field distributions, IA dependence, and structural parameters on this designed metamaterial are included in the process of discussion. This tunable feature enables us to face more complex application environments, which has tremendous research value.

REFERENCES

[1] M. Beruete, M. Navarro-Cia, M. Sorolla, and I. Campillo, "Polarization selection with stacked hole array metamaterial," *J. Appl. Phys.*, vol. 103, no. 5, p. 1353, Mar. 2008.

[2] W. Li, S. Gao, Y. Cai, Q. Luo, M. Sobhy, G. Wei, J. Xu, J. Li, C. Wu, and Z. Cheng, "Polarization-reconfigurable circularly polarized planar antenna using switchable polarizer," *IEEE Trans. Antennas Propag.*, vol. 65, no. 9, pp. 4470–4477, Sep. 2017.

[3] K. Li, Y. Liu, Y. Jia, and Y. J. Guo, "A circularly polarized high-gain antenna with low RCS over a wideband using chessboard polarization conversion metasurfaces," *IEEE Trans. Antennas Propag.*, vol. 65, no. 8, pp. 4288–4292, Aug. 2017.

[4] W. Xu, P. Li, and Y. Qiu, "Electromagnetic performance analysis of inhomogeneous airborne radomes for circular polarization applications," *IEEE Antennas Wireless Propag. Lett.*, vol. 18, no. 1, pp. 74–78, Jan. 2019.

[5] E. Perret, "Displacement sensor based on radar cross-polarization measurements," *IEEE Trans. Microw. Theory Techn.*, vol. 65, no. 3, pp. 955–966, Mar. 2017.

[6] J. Yang and J. Zhang, "Nano-polarization-converter based on magnetic plasmon resonance excitation in an L-shaped slot antenna," *Opt. Express*, vol. 21, no. 7, pp. 7934–7942, Mar. 2013.

[7] W.-S. Chu, S.-M. Kim, X. Wu, L. Wen, and M.-C. Oh, "Optical voltage sensors based on integrated optical polarization-rotated reflection interferometry," *J. Lightw. Technol.*, vol. 34, no. 9, pp. 2170–2174, May 1, 2016.

[8] Y. Su, H. Zhou, Y. Wang, and H. Shen, "A novel polarization demodulation method using polarization beam splitter (PBS) for dynamic pressure sensor," *Opt. Fiber Technol.*, vol. 41, pp. 69–73, Mar. 2018.

[9] R. D. King-Smith and D. Vanderbilt, "Theory of polarization of crystalline solids," *Phys. Rev. B, Condens. Matter*, vol. 47, no. 3, p. 1651, Jan. 1993.

[10] J. A. Davis, I. Moreno, and P. Tsai, "Polarization eigenstates for twisted-nematic liquid-crystal displays," *Appl. Opt.*, vol. 37, no. 5, pp. 937–945, Feb. 2018.

[11] F. Yuan, G. M. Wang, H. X. Xu, T. Cai, X. J. Zou, and Z. H. Pang, "Broadband RCS reduction based on spiral-coded metasurface," *Appl. Phys. Lett.*, vol. 16, pp. 3188–3191, Nov. 2017.

[12] C. Huang, W. Pan, X. Ma, and X. Luo, "Wideband radar cross-section reduction of a stacked patch array antenna using metasurface," *IEEE Antennas Wireless Propag. Lett.*, vol. 14, pp. 1369–1372, Feb. 2015.

[13] R. Panwar, S. Puthucheri, D. Singh, and V. Agarwala, "Design of ferrite-graphene-based thin broadband radar wave absorber for stealth application," *IEEE Tran. Magn.*, vol. 51, no. 11, Jul. 2015, Art. no. 2802804.

[14] L. Zhao, H. Liu, Z. He, and S. Dong, "All-metal frequency-selective absorber/emitter for laser stealth and infrared stealth," *Appl. Opt.*, vol. 57, no. 8, pp. 1757–1764, Jan. 2018.

[15] H.-P. Li, G.-M. Wang, T. Cai, J.-G. Liang, and X.-J. Gao, "Phase- and amplitude-control metasurfaces for antenna main-lobe and sidelobe manipulations," *IEEE Trans. Antennas Propag.*, vol. 66, no. 10, pp. 5121–5129, Oct. 2018.

[16] H. Li, G. Wang, T. Cai, H. Hou, and W. Guo, "Wideband transparent beam-forming metadevice with amplitude-and phase-controlled metasurface," *Phys. Rev. A, Gen. Phys. Appl.*, vol. 11, no. 1, Jan. 2019, Art. no. 014043.

[17] X. Gao, X. Han, W.-P. Cao, H. O. Li, H. F. Ma, and T. J. Cui, "Ultrawideband and high-efficiency linear polarization converter based on double V-shaped metasurface," *IEEE Trans. Antennas Propag.*, vol. 63, no. 8, pp. 3522–3530, Aug. 2015.

[18] Q. Zheng, C. Guo, and J. Ding, "Wideband metasurface-based reflective polarization converter for linear-to-linear and linear-to-circular polarization conversion," *IEEE Antennas Wireless Propag. Lett.*, vol. 17, no. 8, pp. 1459–1463, Aug. 2018.

[19] V. Mishra, R. Panwar, A. Singh, S. Puthucheri, and D. Singh, "Critical analysis of periodic fractal frequency selective surfaces coupled with synthesised ferrite-based dielectric substrates for optimal radar wave absorption," *IET Sci., Meas. Technol.*, vol. 13, no. 6, pp. 794–802, Aug. 2019.

[20] X.-K. Kong, J.-J. Mo, Z.-Y. Yu, W. Shi, H.-M. Li, and B.-R. Bian, "Reconfigurable designs for electromagnetically induced transparency in solid state plasma metamaterials with multiple transmission windows," *Int. J. Mod. Phys. B*, vol. 30, no. 14, Jun. 2016, Art. no. 1650070.
[21] R. Hirota, "Theory of a solid state plasma waveguide in a longitudinal magnetic Field.," *J. Phys. Soc. Jpn.*, vol. 19, no. 12, pp. 2271–2273, Dec. 1964.
[22] D.-J. Kim, J.-S. Park, C. H. Kim, J. Hur, C.-K. Kim, Y.-K. Cho, J.-B. Ko, B. Park, D. Kim, and Y.-K. Choi, "Reconfigurable Yagi-Uda antenna based on a silicon reflector with a solid-state plasma," *Sci. Rep.*, vol. 7, no. 1, p. 17232, Dec. 2017.
[23] F. B. Ashraf, T. Alam, S. Kibria, and M. T. Islam, "A compact meander line elliptic split ring resonator based metamaterial for electromagnetic shielding," *Mater. Express*, vol. 8, no. 2, pp. 133–140, Apr. 2018.
[24] V. Revathi, S. D. Kumar, V. Subramanian, and M. Chellamuthu, "BMFO-PVDF electrospun fiber based tunable metamaterial structures for electromagnetic interference shielding in microwave frequency region," *Eur. Phys. J. Appl. Phys.*, vol. 72, no. 2, p. 20402, Nov. 2015.
[25] Y.-P. Li, H.-F. Zhang, T. Yang, T.-Y. Sun, and L. Zeng, "A multifunctional polarization converter base on the solid-state plasma metasurface," *IEEE J. Quantum Electron.*, vol. 56, no. 2, pp. 1–7, Apr. 2020.
[26] P. C. Wu, W. Zhu, Z. X. Shen, P. H. J. Chong, W. Ser, D. P. Tsai, and A.-Q. Liu, "Broadband wide-angle multifunctional polarization converter via liquid-metal-based metasurface," *Adv. Opt. Mater.*, vol. 5, no. 7, Feb. 2017, Art. no. 1600938.
[27] S. Kalraiya, R. K. Chaudhary, and M. A. Abdalla, "Design and analysis of polarization independent conformal wideband metamaterial absorber using resistor loaded sector shaped resonators," *J. Appl. Phys.*, vol. 125, no. 13, Apr. 2019, Art. no. 134904.
[28] S. R. Thummaluru, N. Mishra, and R. K. Chaudhary, "Design and analysis of an ultrathin triple-band polarization independent metamaterial absorber," *AEU-Int. J. Electron. Commun.*, vol. 82, pp. 508–515, Dec. 2017.
[29] J. Wang, R. Yang, R. Ma, J. Tian, and W. Zhang, "Reconfigurable multifunctional metasurface for broadband polarization conversion and perfect absorption," *IEEE Access*, vol. 8, pp. 105815–105823, Jun. 2020.
[30] D. H. Luu, N. Van Dung, P. Hai, T. T. Giang, and V. D. Lam, "Switchable and tunable metamaterial absorber in THz frequencies," *J. Sci., Adv. Mater. Devices*, vol. 1, no. 1, pp. 65–68, Mar. 2016.
[31] M. Islam, S. J. M. Rao, G. Kumar, B. P. Pal, and D. Roy Chowdhury, "Role of resonance modes on terahertz metamaterials based thin film sensors," *Sci. Rep.*, vol. 7, no. 1, p. 7355, Aug. 2017.
[32] T. Liu and S.-S. Kim, "Design of wide-bandwidth electromagnetic wave absorbers using the inductance and capacitance of a square loop-frequency selective surface calculated from an equivalent circuit model," *Opt. Commun.*, vol. 359, pp. 372–377, Jan. 2016.
[33] Y. Liu, F. D. Flaviis, and N. G. Alexopoulos, "A thin X-band microwave absorber using a center shorted spiral medium," *IEEE Antennas Wireless Propag. Lett.*, vol. 8, pp. 271–274, Dec. 2009.

LI ZENG was born in Hunan, China, in 1999. He is currently pursuing the degree with the College of Electronic and Optical Engineering and the College of Microelectronics, Nanjing University of Posts and Telecommunications, Nanjing, China. His main research interests include the tunable polarization converter and ultra-broadband absorber.

XING-LIANG TIAN was born in Jiangsu, China, in 1996. He received the B.S. degree in applied physics from the Nanjing University of Posts and Telecommunications, Nanjing, China, in 2018, where he is currently pursuing the M.S. degree in electromagnetic field and microwave technology. His research interest includes tunable metamaterial absorber.

YU-PENG LI was born in Guizhou, China, in 1999. She is currently pursuing the degree with the College of Electronic and Optical Engineering and College of Microelectronics, Nanjing University of Posts and Telecommunications, Nanjing, China. Her main research interest includes tunable metamaterial-based polarization converters.

DAN ZHANG (Member, IEEE) received the B.S. degree in mechanical engineering from the Dalian University of Technology, Dalian, China, in 1999, and the M.S. and Ph.D. degrees in electromagnetic waves and communication engineering from Kyushu University, Fukuoka, Japan, in 2004 and 2007, respectively. He is currently a Professor of electronic and communication engineering with the College of Information Science and Technology, Nanjing Forestry University, China. In 2015, he was introduced to Nanjing Forestry University as a high-level talent. In recent years, more than 60 articles have been published by the first author, and more than 20 patents have been applied for granted. He has been invited by the International Professional Society for many times to preside over international conferences or give academic speeches. He is currently an Associate Editor of *IEICE Electronics Express*, and reviewer of several internationally renowned professional journals. His research has been focused on electromagnetic field theory, microwave and optical technology, and nondestructive testing and imaging.

HAI-FENG ZHANG (Member, IEEE) was born in Jiangxi, China, in 1978. He received the M.Sc. degree in electronics science and technology from Nanchang University, Nanchang, China, in 2008, and the Ph.D. degree from the College of Electronic and Information Engineering, Nanjing University of Aeronautics and Astronautics, Nanjing, China, in 2014.

He is currently working as a Professor with the College of Electronic and Optical Engineering and College of Microelectronics, Nanjing University of Posts and Telecommunications, Nanjing, China. His main research interests include the computational electromagnetics, plasma photonic crystal, plasma stealthy, and electromagnetic properties of metamaterials.